Supporting Information

Versatile Synthesis of Nanosized Ni–CeO_2 Catalysts with Tunable Composition for Power-to-Gas Applications

Mathias Barreau[a,§,*], Fengchen Zhou[a], Anastasia Pappa[a], Bachchar Hadrane[a], Ulrike Küst[b,c], Javier Ivanez[d], Davide Salusso[e], Franck Morfin[d], Laurent Piccolo[d], Jan Knudsen[b,c,f] and Spyridon Zafeiratos[a,*]

[a]*Institut de Chimie et Procédés pour l'Energie, l'Environnement et la Santé (ICPEES), ECPM, UMR 7515 CNRS – Université de Strasbourg, 25 rue Becquerel, 67087 Strasbourg Cedex 02, France*

[b]*Division of Synchrotron Radiation Research, Lund University, Box 118, SE-221 00 Lund, Sweden*

[c]*NanoLund, Lund University, Box 118, SE-221 00 Lund, Sweden*

[d]*IRCELYON, CNRS & Université Lyon 1, Villeurbanne 69100, France*

[e]*European Synchrotron Radiation Facility, CS 40220, Cedex 9 F-38043 Grenoble, France*

[f]MAX IV Laboratory, Lund University, Box 118, SE-221 00 Lund, Sweden

Further details on materials and methods

1. Life Cycle Inventory (LCI) Setup

To enable the LCA, a complete life cycle inventory (LCI) of the synthesis was established, covering chemicals, solvents, emissions, and energy inputs. Since many laboratory materials were absent from databases, custom processes were created by tracing their life cycles from literature and supplier data. This ensured accurate modelling of both the catalyst and the reused supernatant streams. To accurately represent the process, a detailed list of all the materials and their exact quantities used in the synthesis was created. This included chemicals, emissions (to air and water), and electricity requirements, served as inputs for modelling the necessary processes. Most of the materials used in the chemical laboratory synthesis were not available in existing databases and therefore had to be added as custom processes. To do so, the entire life cycle of each material was traced consulting bibliography and supplier data. The inventory was divided into segments to allow easier management and dynamic adjustment. First, all the chemicals involved in the synthesis had to be modelled from scratch so they could be used in the creation of Ce-III and Ni-II complexes, which, in combination with oleylamine would form the final catalyst. Subsequently, two processes were defined: one representing the catalyst (final product) and another representing the supernatant, which was reused in the subsequent synthesis cycle following the addition of methanol, as outlined in the synthesis protocol in Figure 1. Among all the available

materials, those that used the “cut-off” method to assess their impacts were selected. This method assigns the environmental burdens of the system to the main output, excluding by-products or secondary products. SimaPro offers a wide range of materials through its databases, covering different geographic regions. Given the context of this study, France was selected as the origin for the inputs in materials when available, while European data was used otherwise. Special attention was paid to the order of the materials to avoid creating loops that would complicate our process tree representation. Because many foreground materials were modelled as custom processes without defined uncertainty ranges, the LCA results are reported without statistical uncertainty analysis.

2. Ambient Pressure X-ray Photoelectron Spectroscopy (APXPS) experiments at the MAX IV synchrotron radiation facility.

APXPS measurements were conducted across two independent beamtimes, yielding fully consistent trends under all tested conditions. Measurements were carried out using a Scienta Omicron HiPP-3 electron analyzer equipped with a 2D CCD-type detector and operating in a cell-in-cell configuration, where the sample is housed within a dedicated ambient pressure cell (inner volume ca. 200 mL). Approximately 10 mg of catalyst powder were pressed into pellets and mounted on a transferrable 304L stainless steel sample plate. The sample was heated using a PID-controlled infrared laser directed at the rear of the plate, with temperature monitored via a type K thermocouple welded to the plate near the sample. Spectra were acquired with a pass energy of 100 eV, using the analyzer in fixed mode. Gases were introduced via calibrated mass flow controllers (Brooks GF125), and the reaction cell pressure was monitored at the outlet using a Baratron capacitance gauge. The gas phase above the catalyst was sampled through the orifice of the analyzer entrance cone, and the composition near the catalyst surface was monitored using a quadrupole mass spectrometer (QMS, Hiden HAL/3F PIC) connected to the first differential pumping stage of the analyzer. Signals corresponding to m/z = 2 (H_2), 15 (CH_4), 18 (H_2O), 28 (CO), 32 (O_2), and 44 (CO_2) were recorded, and signal overlap (e.g., CO contribution to m/z = 28) was corrected based on prior QMS calibration. The collected APXPS spectra included survey scans, Ce 3d, Ni 2p, O 1s, C 1s, and the Fermi edge, using incident photon energies selected to produce photoelectrons with a kinetic energy of ~180 eV, corresponding to comparable information depth across elements. The C 1s binding energy was referenced to the C–C component at 284.8 eV, calibrated via the Fermi edge of samples containing metallic Ni. Spectral background subtraction and peak area integration were performed using CasaXPS software (Casa Software Ltd., version 2.3.25). Atomic concentrations were calculated following normalization to the photon flux and the respective photoionization cross sections. The Ce 3d and Ni $2p_{3/2}$ regions were deconvoluted using internally acquired reference spectra corresponding to Ce^{3+}, Ce^{4+}, Ni^{2+}, and metallic Ni (Ni^0). No differential

charging was observed, as ion compensation in APXPS efficiently neutralizes surface charging. Before acquisition, the catalyst was allowed to equilibrate for 5–10 min under the reaction atmosphere with the beam shutter closed, and the Ce 3d and Ni 2p regions recorded at the beginning and end of each measurement cycle were essentially identical, confirming the absence of significant beam-induced effects.

3. X-Ray Absorption experiments (XAS) at the European Synchrotron Radiation Facility (ESRF).

The XAS Ni K-edge spectra were collected in transmission mode on mass optimized pellets of Ø ≈ 13 mm. A Si coated double reflection mirror was used for harmonic rejections while a Si(111) Double Christal Monochromator (DCM) was used for energy selection. Spectra from the samples were collected with three ion chambers (30 cm) filled with 1.248 mbar of N_2 (I_0) or 0.271 mbar of Ar (I_1/I_2) and topped up to 2 bar with He. The sample pellets were placed between I_0 and I_1 while a Ni metal foil was placed between I_1 and I_2 and used for energy alignment. In-situ spectra were collected on a mass optimized pellet using the Microtomo reactor cell [1]. The sample underwent three heating/cooling steps. The first step consisted in i) heating to 400^{o}C (15^{o}C/min heating ramp rate) under H_2 (20% in He, 50 mL/min total flow), ii) holding at 400^{o}C/H_2 for 30 minutes, iii) cooling to 100^{o}C under H_2 and lastly iv) purging H_2 with pure He flow at 100^{o}C. The same step was then repeated under O_2 (20% in He) (i.e. heating-holding-cooling-purging) and finally again under H_2 (20% in He). The reported spectra NiCe[0.5]-reduced, NiCe[0.5]-oxidized and NiCe[0.5]-2nd_reduced were collected during the final He purging at 100^{o}C of each protocol. Data treatment i.e. energy calibration and alignment, background subtraction and edge jump normalization, were conducted with a dedicated Python script based on the Larch library. [2] Fourier Transform (FT) was applied to the 2-12 $Å^{-1}$ k-range using an Hanning window. FT-EXAFS fit was performed using the Artemis software from the Demeter package. [3]

XRD and Raman results

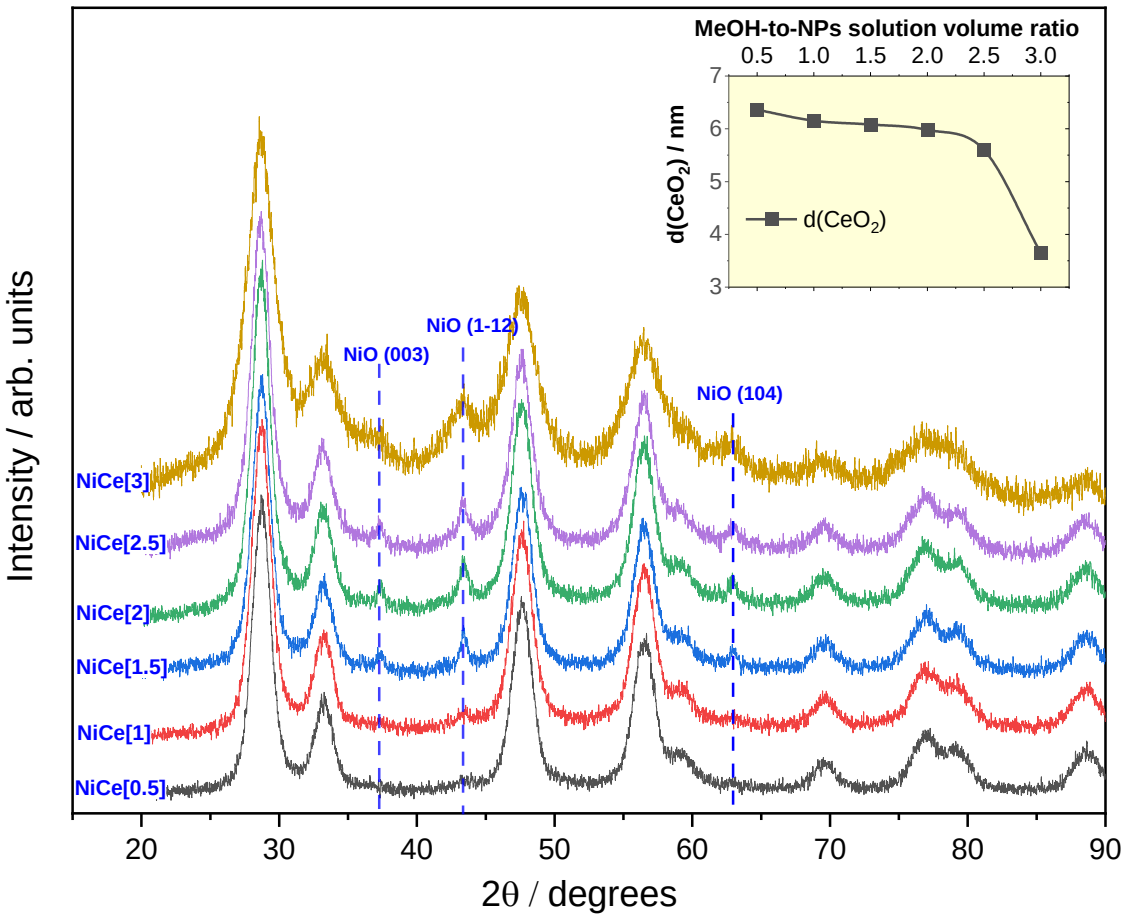

Figure S 1. XRD patterns of $NiCeO_2$ catalysts synthesized using different MeOH-to-NPs solution volume ratios during the precipitation step. The inset shows the evolution of CeO_2 crystallite size, calculated using the Rietveld method.

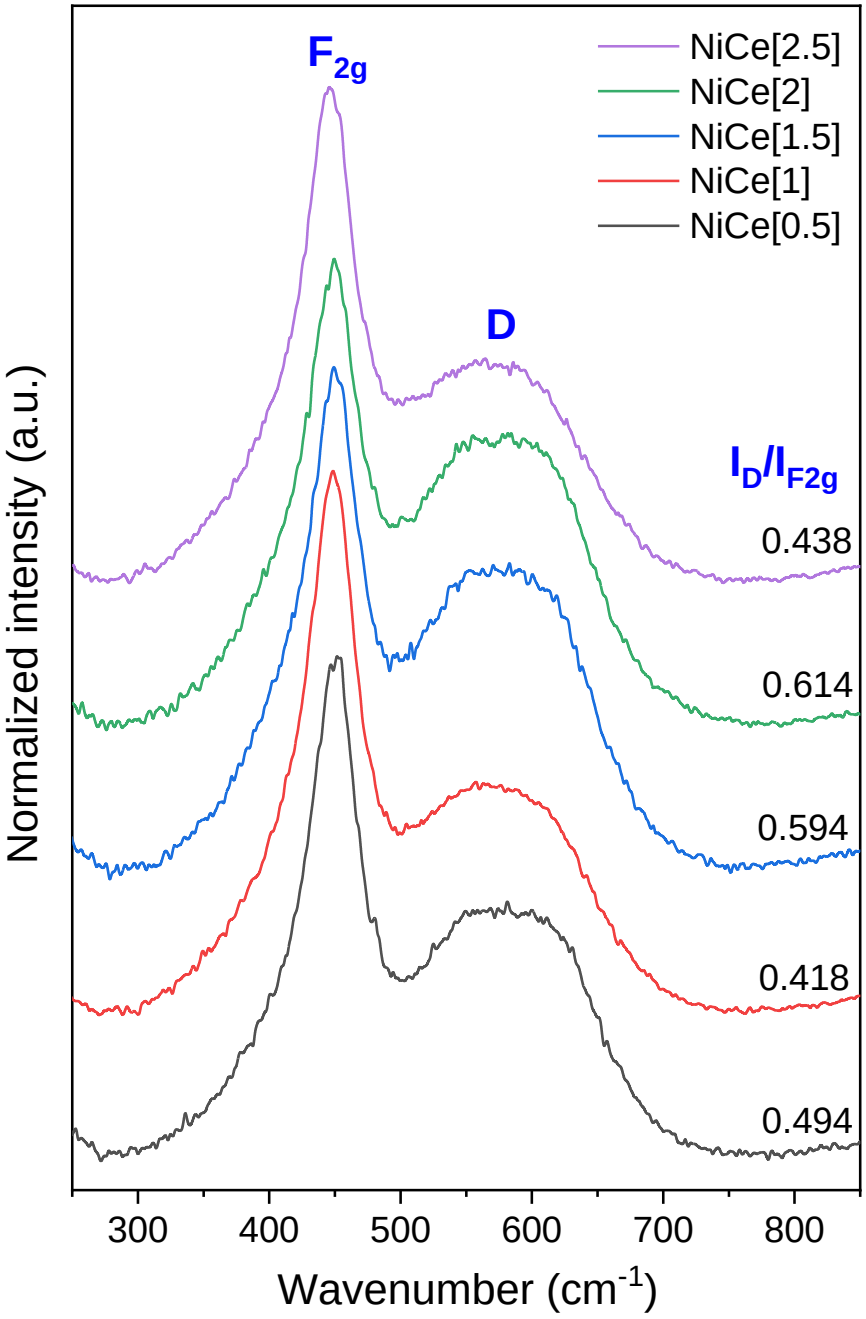

Figure S 2. Raman spectra of the calcined Ni-CeO_2 catalysts recorded with a 532 nm laser.

XAS results

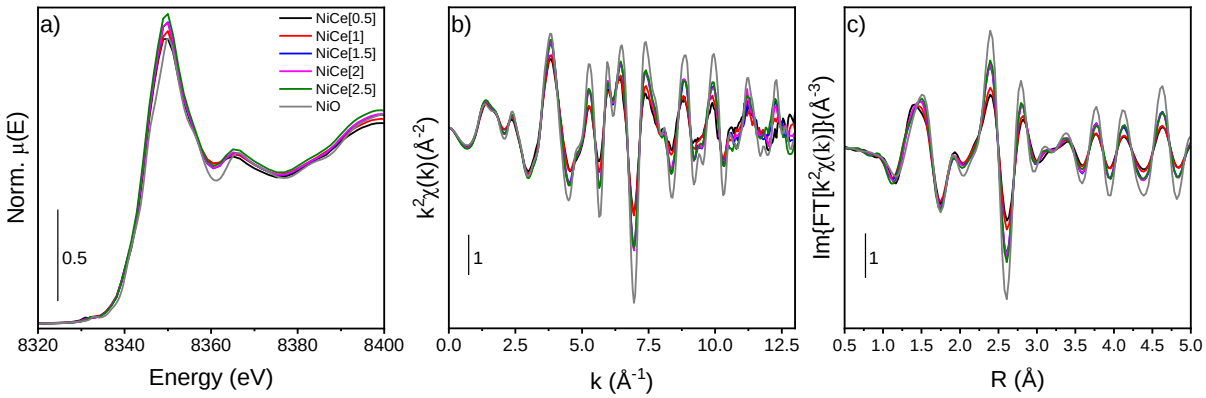

Figure S 3. Ex-situ Ni K-edge a) XANES, b) EXAFS and c) phase uncorrected FT-EXAFS imaginary components spectra.

	NiO	NiCe[0.5]	NiCe[1]	NiCe[1.5]	NiCe[2]	NiCe[2.5]
R-factor	0.009	0.04	0.03	0.02	0.02	0.002
$N_{var}(N_{ind})$	6(12)	5(12)	5(12)	5(12)	5(12)	5(12)
S_0^2	0.99 ± 0.09	1*	1*	1*	1*	1*
ΔE_0 (eV)	-3.3 ± 0.9	-1.2 ± 1.7	-1.4 ± 1.3	-2.0 ± 1.3	-2.0 ± 1.2	-2.2 ± 1.3
CN_{Ni-O}	6	4.4 ± 0.5	4.5 ± 0.4	4.9 ± 0.5	5.0 ± 0.5	5.2 ± 0.5
R_{Ni-O} (Å)	2.077 ± 0.010	2.078 ± 0.018	2.068 ± 0.014	2.071 ± 0.014	2.072 ± 0.013	2.070 ± 0.014
σ^2_{Ni-O} (Å)	0.0073 ± 0.0016	0.007*	0.007*	0.007*	0.007*	0.007*
CN_{Ni-Ni}	12	5.8 ± 0.6	6.4 ± 0.5	8.5 ± 0.6	8.6 ± 0.6	8.9± 0.7
R_{Ni-Ni} (Å)	2.957 ± 0.007	2.983 ± 0.013	2.979 ± 0.010	2.987 ± 0.009	2.970 ± 0.008	2.967 ± 0.009
σ^2_{Ni-Ni} (Å)	0.0069 ± 0.0007	0.007*	0.007*	0.007*	0.007*	0.007*

Table S 1. FT-EXAFS fit results. * indicates values that were fixed. S_0^2 and σ^2 of Ni-CeO_2 samples were fixed to the values obtained for NiO fit. For all the spectra FT-EXAFS was calculated in the 2.46 – 11.7 $Å^{-1}$ k-range while fit was performed in the 1 – 3.1 Å R-range.

Characterization of Co-CeO_2 and CeO_2 samples

MeOH-to-NPs solution volume ratio	Designation	Yield (%)	d_{CeO2} [1] (nm)	d_{Co3O4} [1] (nm)	*BET surface area* (m^2/g)	%Co (± 0.5 wt.%, XPS)	%Co (± 0.5 wt.%, EDX)
0.5	CoCe[0.5]	3	6.68 ± 0.12		116.6		4.2
1.0	CoCe[1]	12	6.65 ± 0.12	7 ± 1	104.5	3.2	4.7
2.0	CoCe[2]	13	7.08 ± 0.13	8 ± 1	84.3	6.1	9.1
4	CoCe[4]	44	7.49 ± 0.13	8.10 ± 0.02	70	15.7	15.1
8	CoCe[8]	20	7.44 ± 0.13	8.2 ± 0.6		16.0	18.7

Table S 2. Summary of synthesis yield and characterization data for Co–CeO_2 catalysts.

MeOH-to-NPs solution volume ratio	Designation	Yield (%)	d_{CeO2}[1] (±1 nm)	*BET surface area* (m^2/g)
1.0	Ce[1]	21.9	9.0 **± 0.3**	91
1.5	Ce[1.5]	43.2	8.8 **± 0.2**	91
2.0	Ce[2]	8.4	9.1 **± 0.2**	76
3.0	Ce[3]	2.4	8.5 **± 0.2**	99

Table S 3. Summary of synthesis yield and characterization data for pure CeO_2 materials.

[1] Determined from XRD data using the Rietveld method.

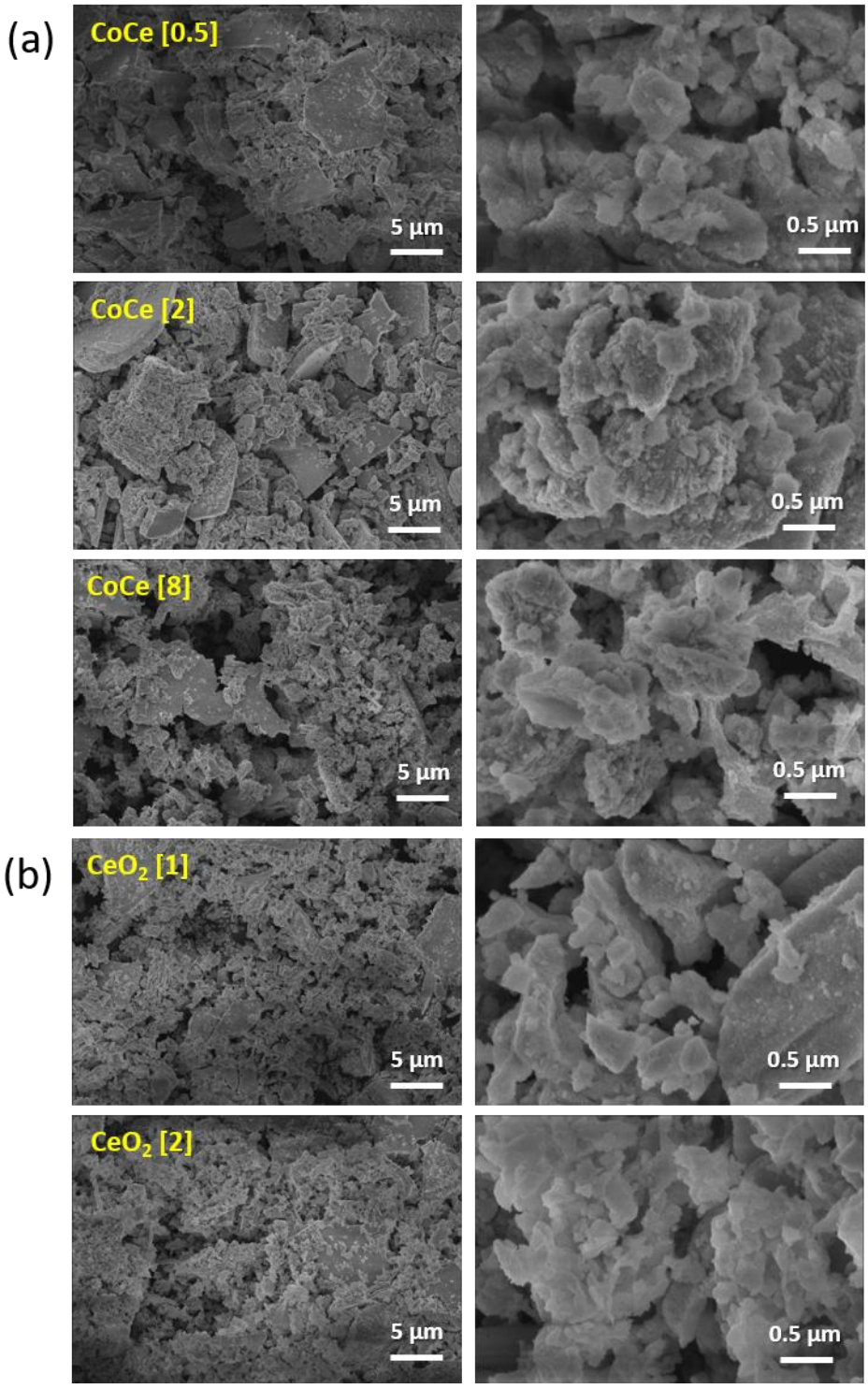

Figure S 4. Representative SEM micrographs of CoCe[x] and CeO_2[x] samples after calcination, shown at magnifications of 5 µm and 0.5 µm.

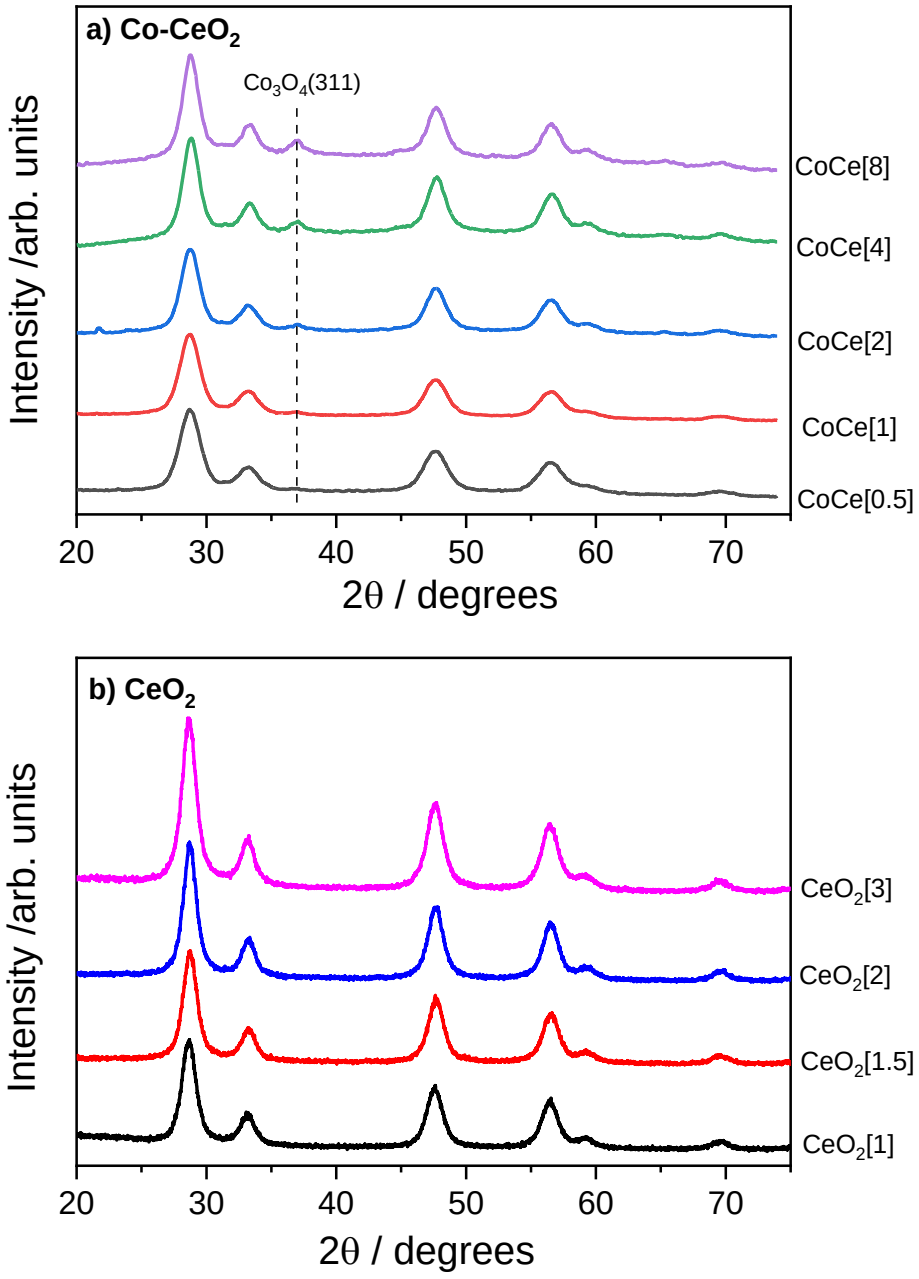

Figure S 5. XRD patterns of (a) Co-CeO_2 and (b) pure CeO_2 powders synthesized using different MeOH-to-NPs solution volume ratios during the precipitation step.

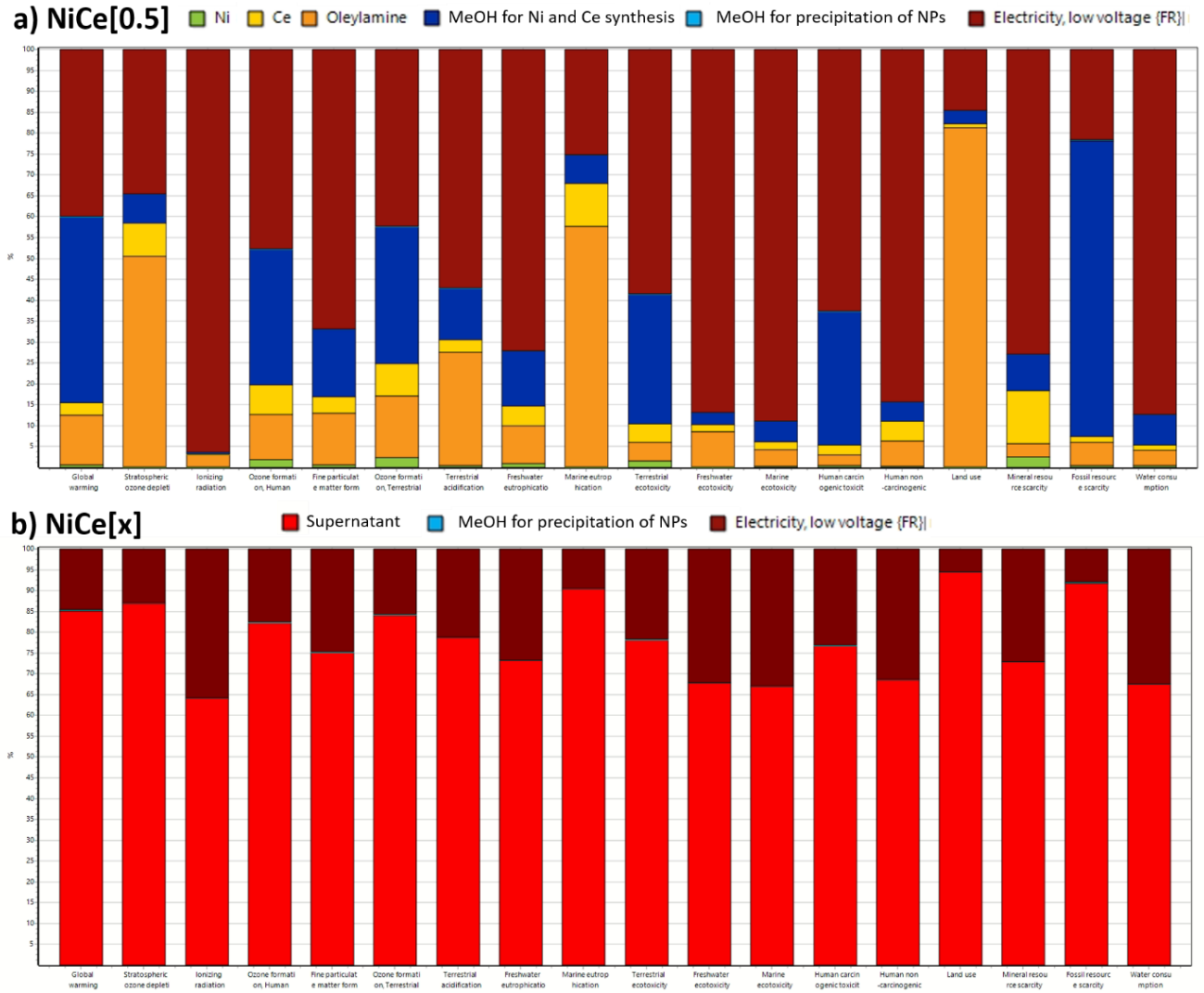

Figure S 6. Contribution analysis of different inputs across 18 environmental impact categories in the LCA of a) NiCe[0.5] and b) NiCe[x] (which combines all catalysts with x ranging from 0.5 to 3) catalyst synthesis. Results are normalized to 100% within each impact category to illustrate the relative contributions of: Ni(II)-L and Ce(III)-L complex preparation, oleylamine and methanol usage, and electricity consumption in various processes (e.g., heating, centrifugation).

Se	Impact category	Unit	NiCe-0.5	NiCe-1	NiCe-1.5	NiCe-2	NiCe-2.5	NiCe-3
☑	Global warming	kg CO2 eq	0.00694	0.00252	0.000957	0.000623	0.000579	0.000577
☑	Stratospheric ozone deplet	kg CFC11 eq	8.33E-9	3.01E-9	1.13E-9	7.37E-10	6.83E-10	6.8E-10
☑	Ionizing radiation	kBq Co-60 eq	0.017	0.00616	0.00231	0.00151	0.0014	0.0014
☑	Ozone formation, Human h	kg NOx eq	1.42E-5	5.15E-6	1.95E-6	1.27E-6	1.18E-6	1.17E-6
☑	Fine particulate matter forr	kg PM2.5 eq	7.3E-6	2.65E-6	9.98E-7	6.5E-7	6.03E-7	6.02E-7
☑	Ozone formation, Terrestria	kg NOx eq	1.67E-5	6.06E-6	2.29E-6	1.49E-6	1.39E-6	1.38E-6
☑	Terrestrial acidification	kg SO2 eq	2.28E-5	8.26E-6	3.11E-6	2.03E-6	1.88E-6	1.87E-6
☑	Freshwater eutrophication	kg P eq	1.73E-6	6.27E-7	2.36E-7	1.54E-7	1.43E-7	1.42E-7
☑	Marine eutrophication	kg N eq	1.52E-6	5.5E-7	2.06E-7	1.34E-7	1.24E-7	1.24E-7
☑	Terrestrial ecotoxicity	kg 1,4-DCB	0.084	0.0304	0.0115	0.00748	0.00695	0.00693
☑	Freshwater ecotoxicity	kg 1,4-DCB	0.00132	0.000477	0.000179	0.000117	0.000109	0.000108
☑	Marine ecotoxicity	kg 1,4-DCB	0.00162	0.000586	0.000221	0.000144	0.000133	0.000133
☑	Human carcinogenic toxici	kg 1,4-DCB	0.00126	0.000457	0.000172	0.000112	0.000104	0.000104
☑	Human non-carcinogenic t	kg 1,4-DCB	0.0145	0.00524	0.00197	0.00128	0.00119	0.00119
☑	Land use	m2a crop eq	0.00111	0.000401	0.000151	9.78E-5	9.05E-5	9E-5
☑	Mineral resource scarcity	kg Cu eq	6.8E-5	2.46E-5	9.27E-6	6.03E-6	5.6E-6	5.59E-6
☑	Fossil resource scarcity	kg oil eq	0.00396	0.00143	0.000544	0.000354	0.000329	0.000329
☑	Water consumption	m3	0.000122	4.44E-5	1.67E-5	1.09E-5	1.01E-5	1.01E-5

Table S 4 Table of environmental impacts among the different Ni-CeO_2 catalysts across different impact categories

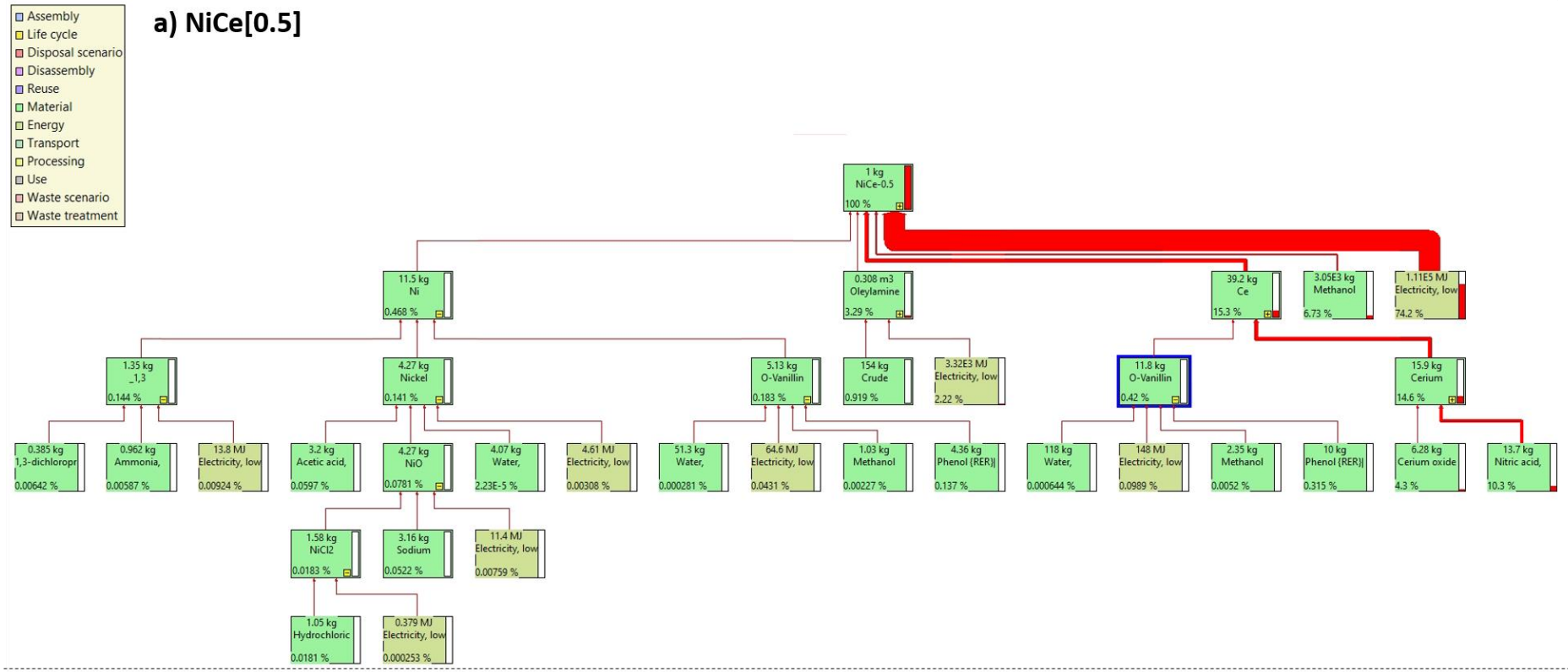
Assembly
Life cycle
Disposal scenario
Disassembly
Reuse
Material
Energy
Transport
Processing
Use
Waste scenario
Waste treatment
a) NiCe[0.5]
1 kg NiCe-0.5 100 %
11.5 kg Ni 0.468 %
0.308 m3 Oleylamine 3.29 %
39.2 kg Ce 15.3 %
3.05E3 kg Methanol 6.73 %
1.11E5 MJ Electricity, low 74.2 %
1.35 kg _1,3 0.144 %
4.27 kg Nickel 0.141 %
5.13 kg O-Vanillin 0.183 %
154 kg Crude 0.919 %
3.32E3 MJ Electricity, low 2.22 %
11.8 kg O-Vanillin 0.42 %
15.9 kg Cerium 14.6 %
0.385 kg 1,3-dichloropr 0.00642 %
0.962 kg Ammonia, 0.00587 %
13.8 MJ Electricity, low 0.00924 %
3.2 kg Acetic acid, 0.0597 %
4.27 kg NiO 0.0781 %
4.07 kg Water, 2.23E-5 %
4.61 MJ Electricity, low 0.00308 %
51.3 kg Water, 0.000281 %
64.6 MJ Electricity, low 0.0431 %
1.03 kg Methanol 0.00227 %
4.36 kg Phenol {RER}| 0.137 %
118 kg Water, 0.000644 %
148 MJ Electricity, low 0.0989 %
2.35 kg Methanol 0.0052 %
10 kg Phenol {RER}| 0.315 %
6.28 kg Cerium oxide 4.3 %
13.7 kg Nitric acid, 10.3 %
1.58 kg NiCl2 0.0183 %
3.16 kg Sodium 0.0522 %
11.4 MJ Electricity, low 0.00759 %
1.05 kg Hydrochloric 0.0181 %
0.379 MJ Electricity, low 0.000253 %

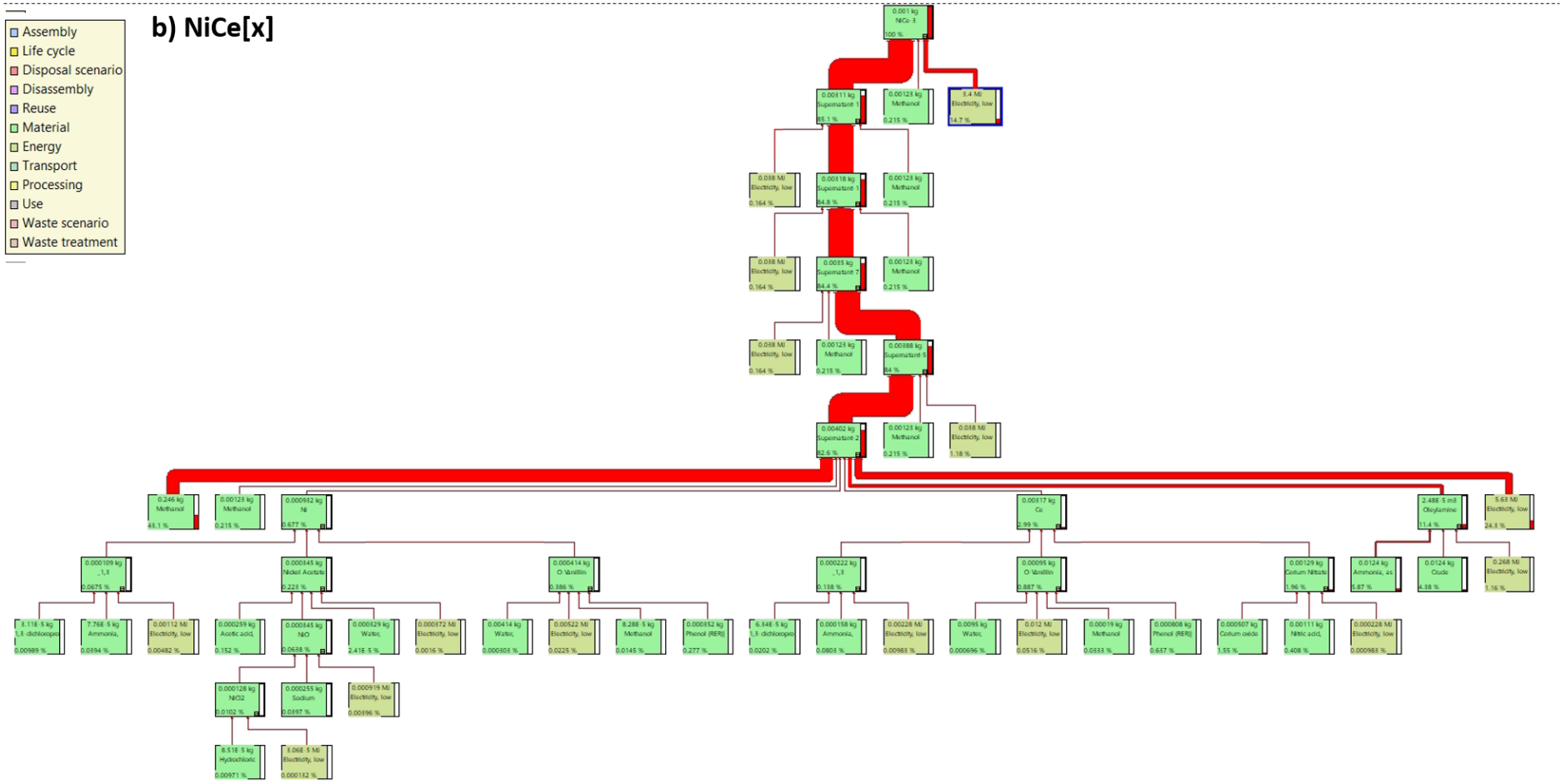

Figure S 7 Tree representation of the a) NiCe[0.5] and b) NiCe[x] (which combines all catalysts with x ranging from 0.5 to 3) catalyst synthesis.

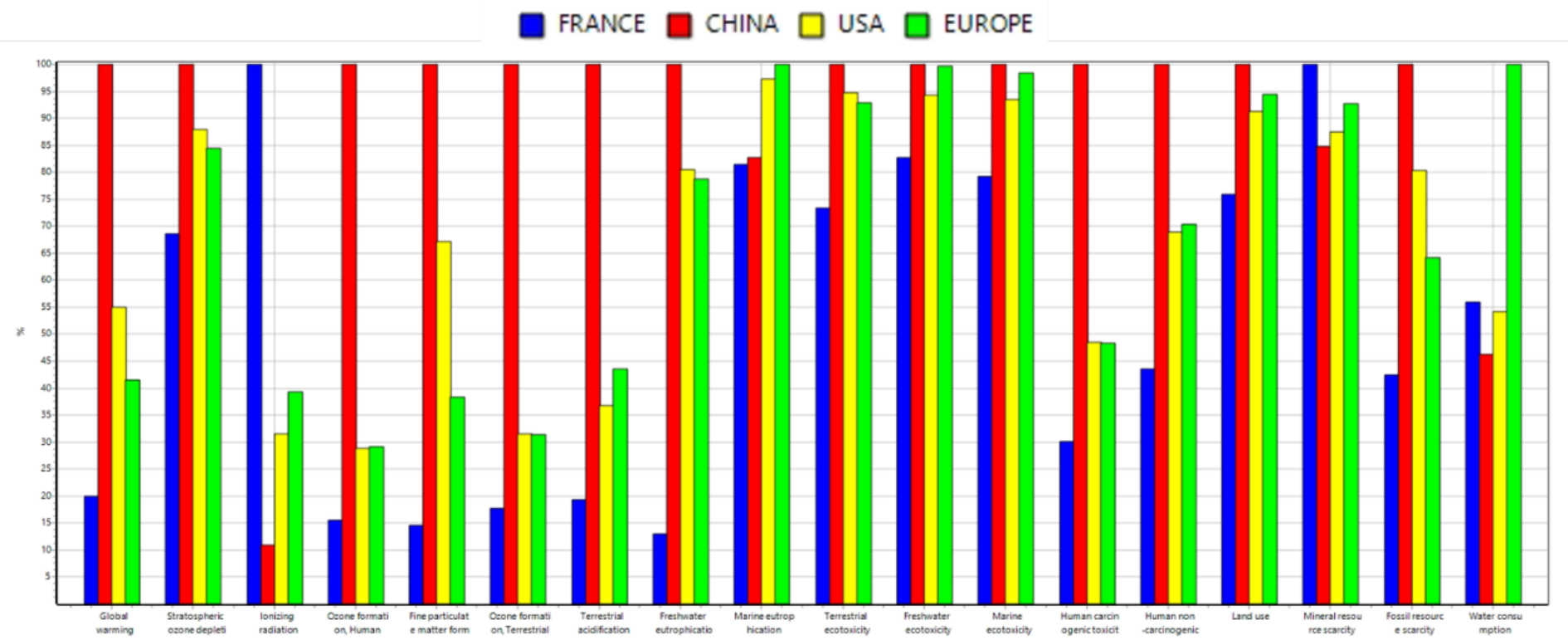

Figure S 8. Sensitivity analysis: Comparison of the contribution of French, Chinese, American, and European electricity mixes across 18 impact categories

H_2-TPR

Sample	H_2 consumption (mmol.g^{-1})				Total H_2 cons. 150 – 400°C	Theo. Ni H_2 cons.
	150-265°C	265-420°C	420-600 °C	600-900 °C		
NiCe[0.5]	0.66	0.73	0.13	0.58	1.39	1.11
NiCe[1]	0.72	1.30	0.08	0.60	2.01	1.53
NiCe[1.5]	0.63	1.76	-	0.59	2.39	2.06
NiCe[2]	0.73	2.14	-	0.56	2.87	2.30

Table S 5. Hydrogen consumption of Ni-CeO_2 catalysts measured by H_2-TPR

Benchmarking Catalyst Performance in the CO_2 Methanation Reaction

Catalyst	Ni content (wt%)	CO_2 Conversion (%)	CH_4 selectivity (%)	WHSV (mL h^{-1} g^{-1})	Temperature (°C)	Reference
NiCe[2]	13.5	90	~100	60000	300	This work
Ni/CeO_2-NR	14	~78	99	30000	300	[4]
Ni-CeO_2-650	15	90	~100	36000	300	[5]
Ni/(0.06AB)CeO_2	9.7	84	99	36000	300	[6]
Ni/CeO_2 (P-60)	9.5	73	93	30000	260	[7]
8Ni-20Ce-CNT	8.4	82	98	26000	290	[8]
Ni/CeO_2-R	8.92	~90	99	20000	300	[9]
Ni/CeO_2-OV-R	10	85	~100	20000	300	[10]
NiNPs@CeO_2NF	10	82.3	98.2	36000	300	[11]
10Ni/CeO_2-M-1	10	78	~100	45000	300	[12]
Ni/CeO_2–Ov	4.9	65	96	30000	300	[13]
Ni/CeO_2-6M	5	58	97.5	36000	300	[14]
8.5%Ni/CeO_2	8.5	50	98	15000	300	[15]
Ni-CeO_2/hBFS	10.2	81.6	99.8	12000	350	[16]
Ni/CeO_2-BTC	10	58	86	72000	350	[17]
Ni/$Ca_{0.1}Ce_{0.9}O_x$	9.15	75	99	36000	300	[18]
10Ni/CeO_2-La-600	10	88.6	88.6	30000	300	[19]
Ni-Pr/CeO_2	8.6	87	~100	25000	300	[20]
20Ni15Mn/Al_2O_3	20	75.1	99.6	30000	300	[21]
Ni/c-ZrO_2	10	62	99	36000	250	[22]
Ni@Y_2O_3	15	78	~100	15000	280	[23]

Table S 6 Catalytic performance of representative Ni/CeO_2 catalysts over CO_2 methanation

Effect of the low-pressure APXPS conditions at the reactivity of the catalysts

APXPS is a very powerful technique for analysing the surface chemistry of materials in contact with reactants, but its operation is restricted in the mbar pressure regime. The CO_2 methanation reaction, however, is sensitive to pressure, and its performance—both in terms of activity and selectivity—is expected to be influenced at the mbar pressure regime compared to the catalytic tests performed at 1 bar. In particular, according to Le Chatelier's principle, decreasing the pressure below 1 bar shifts the reaction equilibrium toward the reactants, as the forward methanation reaction involves a net decrease in the number of gas molecules (from 5 to 3). As a result, lowering the pressure reduces the thermodynamic driving force for CH_4 formation, leading to lower CO_2 conversion. Furthermore, low pressure can negatively impact CH_4 selectivity. The primary competing side reaction in methanation, the RWGS, converts CO_2 to CO and H_2O without a net change in gas volume. Therefore, at lower pressures, RWGS becomes more competitive relative to methanation, especially at lower temperatures where methanation kinetics are slower. This shift results in a decrease in CH_4 production and an increase in CO formation. Overall, the low-pressure conditions inherent to APXPS measurements thermodynamically and kinetically favour a decrease in CO_2 conversion and an increase in the selectivity of the reaction toward CO by suppressing the methanation pathway over RWGS.

Thus, prior to the detailed analysis of the APXPS spectra, the catalytic performance of the NiCe[0.5] and NiCe[2] samples within the APXPS cell was evaluated. This was carried out by combining real-time gas-phase monitoring using a quadrupole mass spectrometer (QMS) and C 1s gas-phase spectral analysis. As shown in Figures S3, both catalysts exhibited a progressive decrease in the CO_2 signal, accompanied by the simultaneous emergence of CO and CH_4 signals with increasing reaction temperature—clear evidence of CO_2 conversion under the applied conditions. A comparison between the two catalysts revealed significant differences in both the extent of CO_2 conversion and the distribution of gaseous products, indicating variations in their catalytic reactivity and selectivity

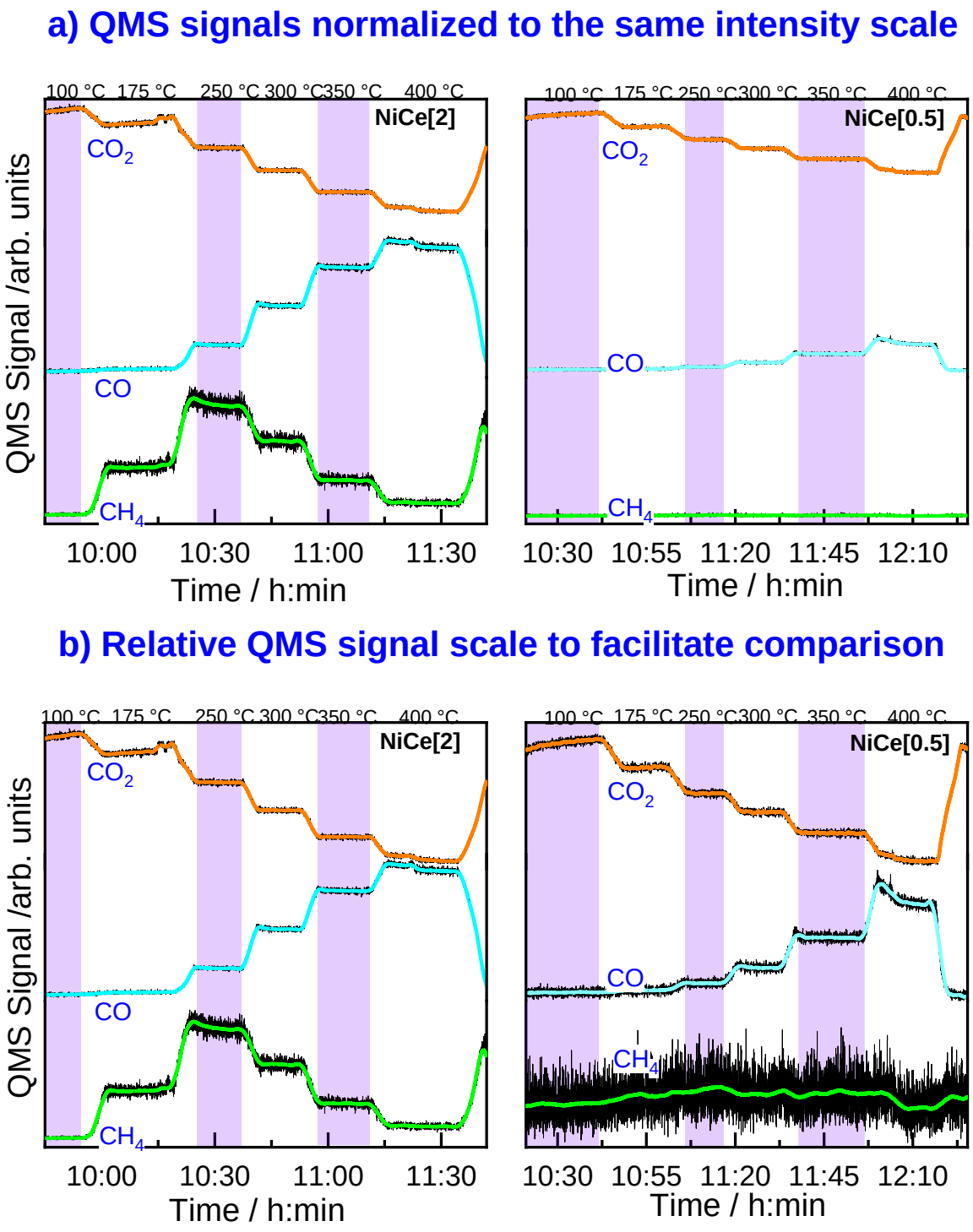

Figure S 9. Quadrupole mass spectrometry (QMS) signals recorded during the CO_2 methanation reaction in the APXPS cell for the NiCe[0.5] and NiCe[2] catalysts. The QMS (connected to the first differential pumping stage of the analyzer) monitored signals at m/z = 15 (CH_4), 28 (CO; corrected for the contribution from CO_2 fragmentation at m/z = 44), and 44 (CO_2). Data are presented (a) normalized to the same intensity scale, and (b) on a relative intensity scale to facilitate comparison of signal features.

Figure S9a presents the X_{CO2} and S_{CH4} derived from the QMS data in the APXPS cell. Notably, differences in X_{CO2} between the two catalysts become apparent above 250 °C, with NiCe[2] displaying significantly higher CO_2 conversion and CH_4 selectivity than NiCe[0.5].

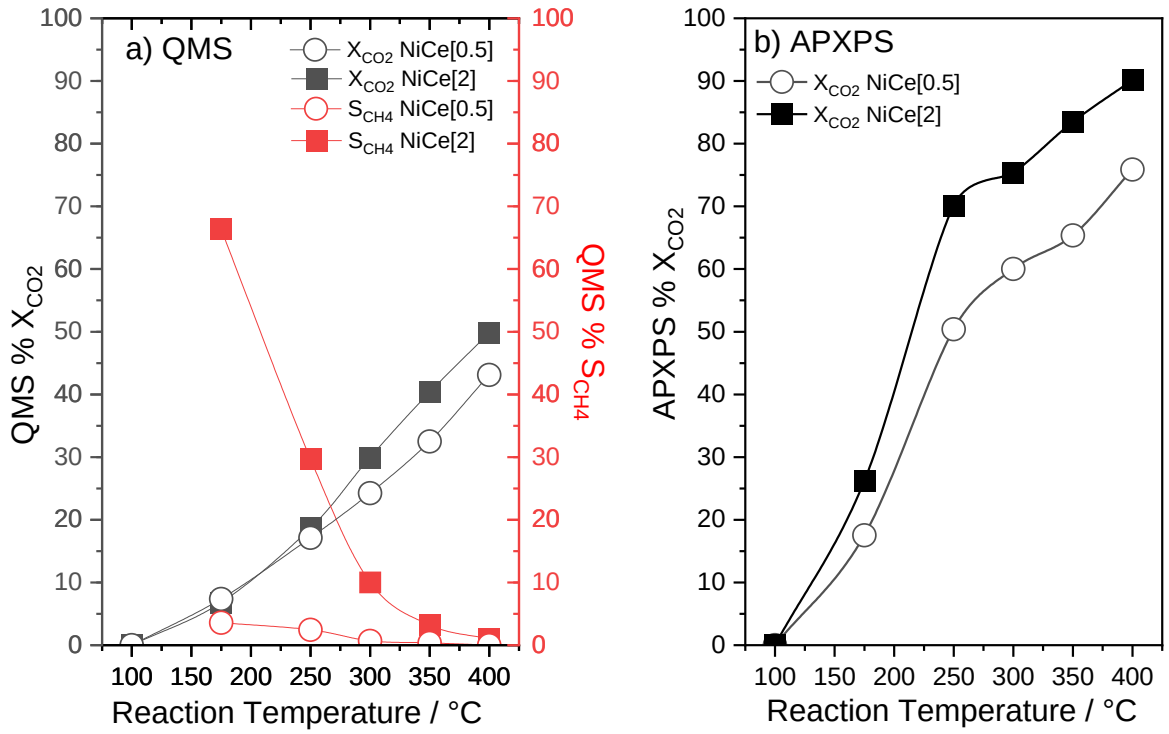

Figure S 10. (a) CO_2 conversion (X_{CO2}) and CH_4 selectivity (S_{CH4}) derived from the QMS signal recorded in the APXPS cell (see Figure S8), (b) CO_2 conversion estimated from the ratio of the CO_2 gas-phase C 1s peak to the Ce 3d peak area, normalized for each sample to its initial value at 100 °C.

In APXPS, gas-phase molecules located immediately above the catalyst surface are photoionized, providing real-time insight into the local reaction environment in close proximity to the catalyst surface. These gas-phase species typically produce sharp, narrow peaks that can be clearly distinguished from the broader signals arising from surface-adsorbed carbon species. Figure S10a shows characteristic gas-phase C 1s spectra acquired under reaction conditions, in which distinct contributions from CO_2 and CO can be clearly identified. By fitting these two features in the C 1s region, the gas-phase signals of CO_2 and CO can be quantified, enabling an indirect estimation of CO_2 consumption and CO formation during the reaction. However, due to the relatively low CH_4 yield the gas-phase CH_4 signal could not be reliably detected under the present experimental conditions. In Figure S10b, the X_{CO2} calculated by the C 1s(CO_2 gas-phase)/Ce 3d peak area ratio and normalized for each sample to its initial value at 100 °C, is consistently higher for the NiCe[2] catalyst compared to NiCe[0.5]. This trend aligns well with the results

in Figure S10a, obtained from QMS analysis. Furthermore, the relative CO production, expressed as the CO/CO_2 gas-phase C 1s peak area ratio (Figure S9b), provides additional evidence that NiCe[2] generates more CO at elevated temperatures than NiCe[0.5].

Overall, the performance of the two catalysts under low-pressure APXPS conditions, as assessed by both QMS and photoemission data, qualitatively follows the trends observed in the catalytic tests conducted at 1 bar. In particular, as shown in Figure 7 of the main text, the NiCe[0.5] catalyst consistently exhibits lower CO_2 conversion and CH_4 selectivity at low temperatures compared to NiCe[2], a behaviour that is reproduced under APXPS conditions. Furthermore, in line with the thermodynamic and kinetic considerations discussed above, both CO_2 conversion and CH_4 selectivity are significantly lower under APXPS conditions than in the atmospheric pressure experiments. This outcome is fully consistent with the expected influence of reduced pressure, which thermodynamically disfavours the formation of CH_4 and kinetically limits reaction rates.

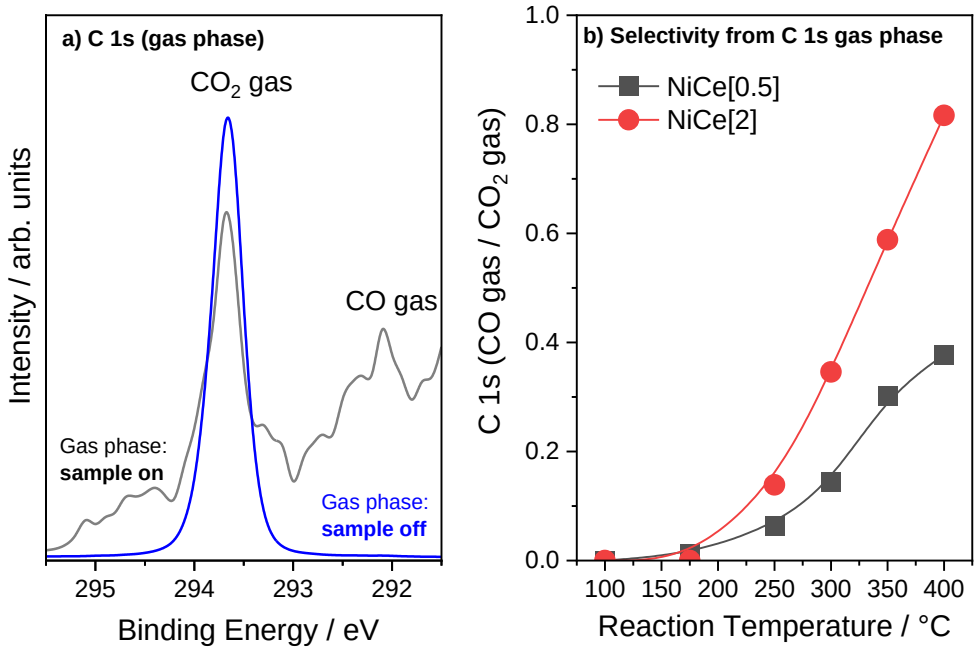

Figure S 11 . (a) APXPS C 1s spectra in the binding energy region corresponding to CO_2 and CO gas-phase photoemission peaks. Both spectra were recorded using a photon energy of 465 eV. The grey spectrum ("sample on") was acquired with the sample positioned at the focal point (measurement position), while the gas-phase spectrum ("sample off") was recorded with the sample retracted by 400 µm from the focal position to minimize surface contributions. (b) Relative CO production of the NiCe[2] and NiCe[0.5] catalysts as a function of reaction temperature, calculated from the CO/CO_2 gas-phase C 1s peak area ratio obtained by APXPS measurements.

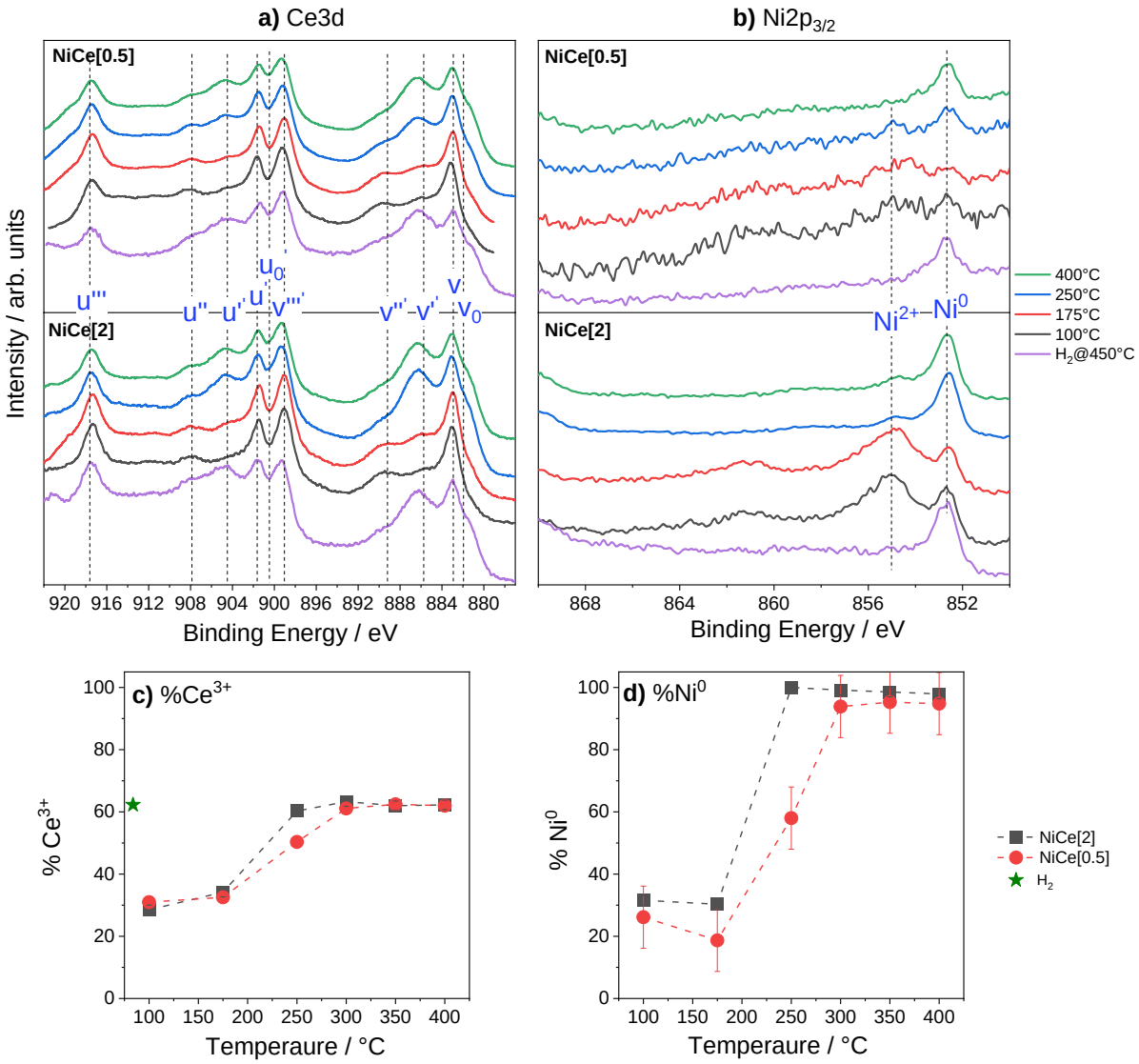

Figure S 12. (a) Ce 3d and (b) Ni $2p_{3/2}$ APXPS spectra of the NiCe[0.5] and NiCe[2] catalysts recorded during H_2 treatment at 450 °C and under CO_2:H_2 atmospheres at four characteristic temperatures. (c) Temperature-dependent evolution of Ce^{3+} and (d) metallic Ni (Ni^0) content, expressed as a percentage of the total Ce 3d and Ni 2p signal areas, respectively. Quantification was performed by fitting the Ce 3d and Ni 2p regions using reference spectra.

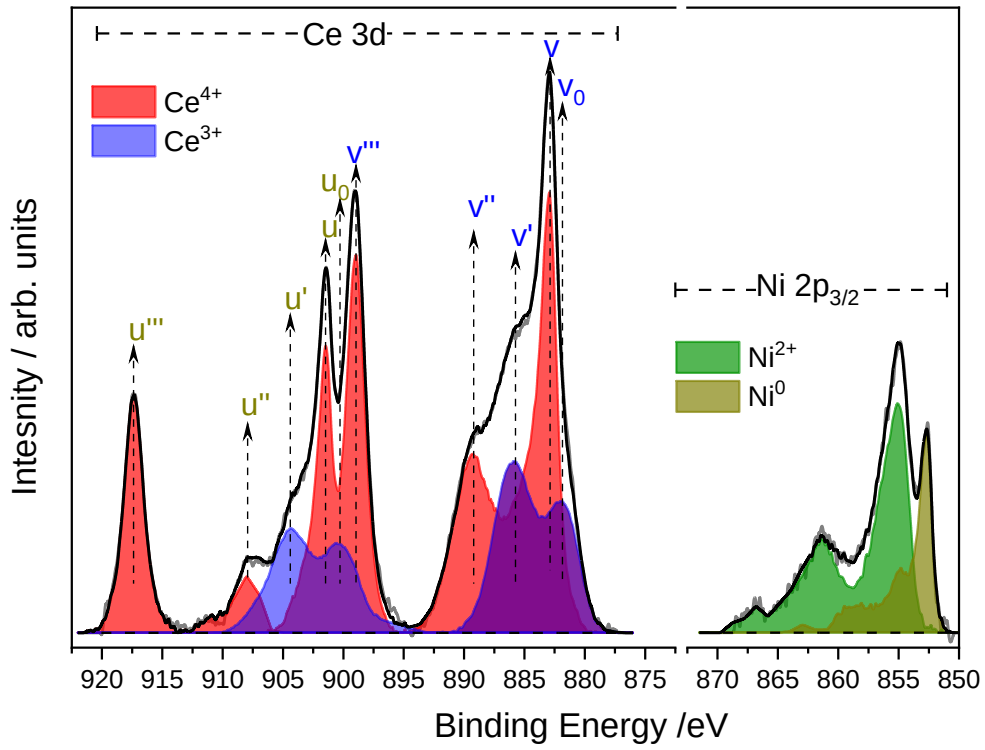

Figure S 13. Representative example of the fitting procedure for the Ce 3d and Ni $2p_{3/2}$ photoemission peaks using reference spectra corresponding to Ce^{3+}, Ce^{4+}, Ni^{2+}, and metallic Ni (Ni^{0}).

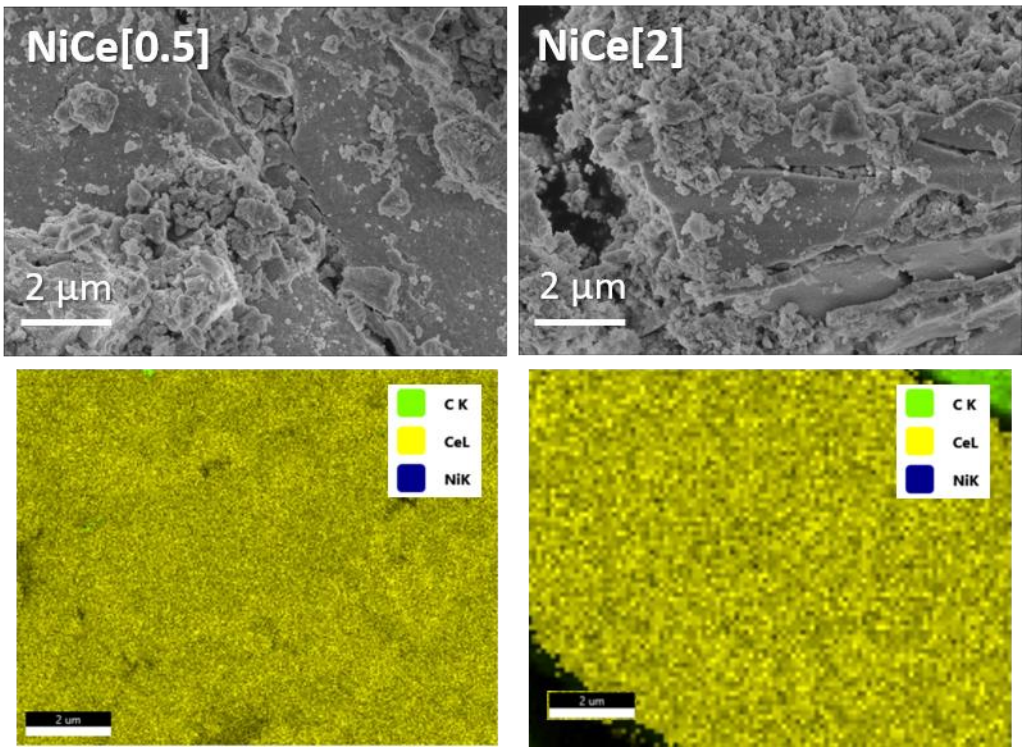

Figure S 14. SEM images (top row) and corresponding SEM/EDX elemental maps (bottom row) of NiCe[0.5] (left) and NiCe[2] (right) catalysts after reactivity testing in the APXPS apparatus. EDX elemental mapping confirms a homogeneous distribution of Ce (yellow) and Ni (blue) at the microscale.

References

1 D. Bellet, B. Gorges, A. Dallery, P. Bernard, E. Pereiro and J. Baruchel, *J Appl Crystallogr*, 2003, **36**, 366–367.

2 M. Newville, *J Phys Conf Ser*, 2013, **430**, 012007.

3 B. Ravel and M. Newville, *J. Synchrotron Rad*, 2005, **12**, 537–541.

4 B. Musig, A. Roy, R. Arenal, T. García, M. E. Gálvez and M. V. Navarro, *Chemical Engineering Journal*, 2024, **479**, 147566.

5 P. Gao, S. Tang, X. Han, Z. Hao, J. Chen, Y. Pan, Z. Zhang, H. Zhang, X. Zi, L. Chen, M. Li and X. Ma, *Chemical Engineering Journal*, 2024, **498**, 155784.

6 X. Chen, R. Ye, C. Sun, C. Jin, Y. Wang, H. Arandiyan, K. H. Lim, G. Song, F. Hu, C. Li, Z. H. Lu, G. Feng, R. Zhang and S. Kawi, *Chemical Engineering Journal*, 2024, **484**, 149471.

7 S. Chen, L. Costley-Wood, I. Lezcano-Gonzalez, E. Campbell, Z. Weng, M. Asunción Molina, Y. Wu and A. M. Beale, *Applied Catalysis B: Environment and Energy*, 2025, **366**, 125029.

8 V. S. Derevschikov, A. P. Suknev, E. M. Sadovskaya, A. Tiurina, D. A. Yatsenko, A. A. Leonova, E. Y. Gerasimov, P. S. Ruvinskiy, S. I. Moseenkov and V. L. Kuznetsov, *Chem Eng Sci*, 2026, **320**, 122515.

9 Y. Xie, J. Chen, X. Wu, J. Wen, R. Zhao, Z. Li, G. Tian, Q. Zhang, P. Ning and J. Hao, *ACS Catal*, 2022, **12**, 10587–10602.

10 W. Yang, K. Chang, M. Yang, X. Yan, S. Yang, Y. Liu, G. Wang, F. Xia, H. Wang and Q. Zhang, *Chemical Engineering Journal*, 2024, **499**, 156493.

11 F. Hu, R. Ye, C. Jin, D. Liu, X. Chen, C. Li, K. H. Lim, G. Song, T. Wang, G. Feng, R. Zhang and S. Kawi, *Appl Catal B*, 2022, **317**, 121715.

12 R. Tang, N. Ullah, Y. Hui, X. Li and Z. Li, *Molecular Catalysis*, 2021, **508**, 111602.

13 X. Qin, Z. Gong, S. Yin, J. Huang, T. Zhang, Q. Liu, L. Dong, P. Zheng and P. Liang, *ACS Sustain Chem Eng*, 2025, **13**, 15223–15232.

14 S. Lin, Z. Li and M. Li, *Fuel*, 2023, **333**, 126369.

15 J. A. Onrubia-Calvo, A. Quindimil, A. Davó-Quiñonero, A. Bermejo-López, E. Bailón-García, B. Pereda-Ayo, D. Lozano-Castelló, J. A. González-Marcos, A. Bueno-López and J. R. González-Velasco, *Ind Eng Chem Res*, 2022, **61**, 10419–10435.

16 X. Chen, Y. He, X. Cui and L. Liu, *Fuel*, 2023, **338**, 127309.

17 M. Dong, J. Wu, J. Yang, H. Liu, X. Chen, Z. Huang and J. Lu, *J Environ Chem Eng*, 2025, **13**, 118575.

18 K. Liu, X. Xu, J. Xu, X. Fang, L. Liu and X. Wang, *Journal of CO2 Utilization*, 2020, **38**, 113–124.

19 T. Zhang, W. Wang, F. Gu, W. Xu, J. Zhang, Z. Li, T. Zhu, G. Xu, Z. Zhong and F. Su, *Appl Catal B*, 2022, **312**, 121385.

20 N. Choudhary, N. Srivastava, H. V. Annadata, B. Ghosh and P. Da Costa, *Small*, 2025, **21**, 2504707.

21 W. Zhang, L. shen, L. Xu, F. Zhou, F. Sun, J. Xu and M. Zhu, *J Catal*, 2025, **448**, 116215.

22 L. Li, X. Wu, H. Cai, J. Yang, J. Zhu, G. Li and C. Hu, *Chemical Engineering Journal*, 2025, **519**, 165036.

23 H. Fan, D. Xu, K. Liu, G. Hou, Y. Li, S. Huang, K. Wu, Y. Xu, R. Shan, Z. Zhang and M. Ding, *Chemical Engineering Journal*, 2025, **503**, 158545.